Probing multirescattering dynamics and electron quantum paths for below- and near-threshold harmonic generation of H_2 in an intense laser field

John Heslar[1] and Shih-I Chu[1,2]

[1]*Department of Physics, Center for Quantum Science and Engineering and Center for Advanced Study in Theoretical Sciences, National Taiwan University, Taipei 10617, Taiwan*

[2]*Department of Chemistry, University of Kansas, Lawrence, Kansas 66045, USA*

(Received 27 December 2016; published 17 April 2017)

Most previous studies of high-order-harmonic generation have focused on the regime beyond the ionization threshold; the dynamical origin of below- and near-threshold harmonics, particularly for the molecular systems, is less understood and largely unexplored. Here, we report a *self-interaction free* time-dependent density-functional-theory study along with an extended semiclassical study for the nonperturbative probing of the dynamical origin of below- and near-threshold harmonic generation of the H_2 molecule in an intense near-infrared laser field. Our approach allows an accurate study of the electron trajectories as a function of energy, time, and position for below-, near-, and above-threshold harmonics for electrons departing initially from each of the individual hydrogen cores of the H_2 molecule. We discover that short trajectories are multiphoton dominated and can have multiple returns for below-threshold harmonics, and excited-state resonances can have significant effects on the generation of neighboring below-threshold harmonics. Furthermore, we find that the electron dynamics for below-threshold long, short, and resonant trajectories differ greatly depending upon which hydrogen core (left or right) the electron was released from initially. An intuitive and appealing picture of near- and below-threshold harmonic generation discovered in our study can give guidance to future experiments in this forefront area of ultrafast atomic, molecular, and optical physics.

DOI: 10.1103/PhysRevA.95.043414

I. INTRODUCTION

High-order-harmonic generation (HHG) is a fundamental atomic and molecular process in strong laser fields that continues to receive considerable attention and plays a crucial role in the development of ultrafast science and technology [1,2]. Significant application of the HHG technology includes the generation of ultrashort attosecond pulses [3–5], frequency combs [6,7], and ultrafast molecular imaging [8,9], to name only a few. The availability of the attosecond pulse further allows the direct detection and control of the electronic dynamics in atoms, molecules, and condensed-matter systems [2,3,5,8–12]. The general pattern of the HHG power spectrum for harmonics above the atoms' or molecules' ionization threshold I_p can be qualitatively explained by means of the three-step model [13,14]. In this scenario, the strong-field approximation (SFA) [15] is effective to explain the process.

More recently, considerable attention has been paid to the near- and below-threshold regimes [6,16–23] as a potential source of coherent vacuum-ultraviolet radiation [2,6]. In these lower-energy regimes, the conventional three-step model and the SFA become inadequate since they neglect the Coulomb potential and the detailed electronic structure of the target atom or molecule. Recently, Xiong *et al.* [20] and Li *et al.* [24–26] have studied the subtle electron dynamics for near- and below-threshold harmonic generation for atoms in strong laser fields. Lately, several studies look into the fact that excited states have effects on the generation of below-threshold harmonics [9,20,27–29], which we recently demonstrated along with the experimentalists [19].

Knowledge of the exact mechanisms for the production of below-, near-, and above-threshold harmonics can give guidance in probing molecular dynamics on an attosecond time scale [9,30]. Recently, the H_2 molecule has been the candidate to study the ultrafast nuclear dynamics on the laser-subcycle time scale [9,30]. Recent studies of H_2 molecules emphasize the importance of time to energy mapping controlled by changing the intensity or wavelength of the laser field [9,30].

In this paper, we present an *ab initio* quantum and extended semiclassical precision study of the below-, near-, and above-threshold harmonic generation of the H_2 molecule in an intense near-infrared (NIR) laser field. Our method allows the accurate probing of the electron paths as a function of energy, time, and position for below-, near-, and above-threshold harmonics for electrons departing initially from each of the individual hydrogen cores of the H_2 molecule. We make use of the *all-electron* time-dependent density functional theory (TDDFT) with proper long-range potentials [31]. In addition, we employ a recently developed synchrosqueezing transform (SST) [25,32–36] to analyze the time-frequency spectra of the below-, near-, and above-threshold HHG of H_2. By comparing the SST time-frequency spectra and the extended semiclassical calculations, we unravel the contributions of the short trajectories, long trajectories, multiscattering trajectories, and resonant trajectories in the below-, near-, and above-threshold harmonic generation for the H_2 molecule.

The paper is organized as follows. In Sec. II, we provide a detailed description of our theoretical approach in the framework of the time-dependent density functional theory (TDDFT) and the time-dependent Schrödinger equation (TDSE) with inclusion of a molecular model potential for the H_2 molecule subject to an intense NIR laser field. In Sec. III, we discuss the results of the *ab initio* quantum and extended semiclassical calculations and give necessary theoretical explanations. Section IV contains concluding remarks.

II. METHOD

A. *Ab initio* TDDFT simulation of the high-order-harmonic generation spectra of the H_2 molecule

Detailed numerical procedures can be found in Refs. [28,37–41]. The basic equations of TDDFT are the time-dependent one-electron Kohn-Sham equations [42] for spin orbitals $\psi_{i\sigma}(\boldsymbol{r},t)$ which involve an effective potential $v_{\mathrm{eff},\sigma}(\boldsymbol{r},t)$ (atomic units $\hbar = m = e = 1$ are used unless stated otherwise),

$$i\frac{\partial}{\partial t}\psi_{i\sigma}(\boldsymbol{r},t) = \left[-\frac{1}{2}\nabla^2 + v_{\mathrm{eff},\sigma}(\boldsymbol{r},t)\right]\psi_{i\sigma}(\boldsymbol{r},t), \quad i = 1,2,\ldots,N_\sigma, \tag{1}$$

where $N_\sigma (= N_\uparrow$ or $N_\downarrow)$ is the total number of electrons for a given spin σ, and the total number of electrons in the system is $N = \sum_\sigma N_\sigma$. The time-dependent effective potential $v_{\mathrm{eff},\sigma}(\boldsymbol{r},t)$ is a functional of the electron spin densities $\rho_\sigma(\boldsymbol{r},t)$ which are related to the spin orbitals as follows:

$$\rho_\sigma(\boldsymbol{r},t) = \sum_{i=1}^{N_\sigma} |\psi_{i\sigma}(\boldsymbol{r},t)|^2 \tag{2}$$

(the summation includes all spin orbitals with the same spin). The effective potential $v_{\mathrm{eff},\sigma}(\boldsymbol{r},t)$ in Eq. (1) can be written in the following general form:

$$v_{\mathrm{eff},\sigma}(\boldsymbol{r},t) = v_{\mathrm{H}}(\boldsymbol{r},t) + v_{\mathrm{ext}}(\boldsymbol{r},t) + v_{\mathrm{xc},\sigma}(\boldsymbol{r},t), \tag{3}$$

where

$$v_{\mathrm{H}}(\boldsymbol{r},t) = \int \frac{\rho(\boldsymbol{r}',t)}{|\boldsymbol{r}-\boldsymbol{r}'|}d\boldsymbol{r}' \tag{4}$$

is the Hartree potential due to electron-electron Coulomb interaction and $\rho(\boldsymbol{r},t)$ is the total electron density,

$$\rho(\boldsymbol{r},t) = \sum_\sigma \rho_\sigma(\boldsymbol{r},t). \tag{5}$$

Here, $v_{\mathrm{ext}}(\boldsymbol{r},t)$ is the "external" potential due to the interaction of the electron with the external laser field and the nuclei. In the case of homonuclear or heteronuclear diatomic molecules in a linearly polarized external laser field $[\boldsymbol{E}(t)\cdot\boldsymbol{r}]$, we have

$$v_{\mathrm{ext}}(\boldsymbol{r},t) = v_n(\boldsymbol{r}) + \boldsymbol{E}(t)\cdot\boldsymbol{r}, \tag{6}$$

where $v_n(\boldsymbol{r})$ is the nuclear potential,

$$v_n(\boldsymbol{r}) = -\frac{Z_1}{|\boldsymbol{R}_1-\boldsymbol{r}|} - \frac{Z_2}{|\boldsymbol{R}_2-\boldsymbol{r}|}. \tag{7}$$

Also, $\boldsymbol{r}$ is the electronic coordinate, $E(t)$ is the electric-field amplitude where the laser field is polarized along the molecular axis, $\boldsymbol{R}_1$ and $\boldsymbol{R}_2$ are the coordinates of the two nuclei at their fixed equilibrium positions, and Z_1 and Z_2 are the electric charges of the two nuclei, respectively. The internuclear separation R is equal to $|\boldsymbol{R}_2 - \boldsymbol{R}_1|$. Finally, $v_{\mathrm{xc},\sigma}(\boldsymbol{r},t)$ is the time-dependent exchange-correlation (XC) potential. Since the exact form of $v_{\mathrm{xc},\sigma}(\boldsymbol{r},t)$ is unknown, the *adiabatic* approximation is often used [37–41,43],

$$v_{\mathrm{xc},\sigma}(\boldsymbol{r},t) = v_{\mathrm{xc},\sigma}[\rho_\sigma]|_{\rho_\sigma=\rho_\sigma(\boldsymbol{r},t)}. \tag{8}$$

When these potentials, determined by the time-independent ground-state density functional theory (DFT), are used along with TDDFT in the electronic structure calculations, both inner shell and excited states can be calculated rather accurately [44]. In this work, we utilize the improved van Leeuwen–Baerends LB94 XC potential [31]. The LB94 contains two empirical parameters α and β and has the following explicit form, in the adiabatic approximation:

$$v_{\mathrm{xc},\sigma}^{\mathrm{LB94}}(\boldsymbol{r},t) = \alpha v_{\mathrm{x},\sigma}^{\mathrm{LSDA}}(\boldsymbol{r},t) + v_{\mathrm{c},\sigma}^{\mathrm{LSDA}}(\boldsymbol{r},t) - \frac{\beta x_\sigma^2(\boldsymbol{r},t)\rho_\sigma^{1/3}(\boldsymbol{r},t)}{1+3\beta x_\sigma(\boldsymbol{r},t)\ln\left\{x_\sigma(\boldsymbol{r},t)+\left[x_\sigma^2(\boldsymbol{r},t)+1\right]^{1/2}\right\}}. \tag{9}$$

Here, ρ_σ is the electron density with spin σ, and we use $\alpha = 1$ and $\beta = 0.05$ [38–41]. The first two terms in Eq. (9), $v_{\mathrm{x},\sigma}^{\mathrm{LSDA}}$ and $v_{\mathrm{c},\sigma}^{\mathrm{LSDA}}$, are the local spin-density approximation (LSDA) exchange and correlation potentials that do *not* have the correct Coulombic asymptotic behavior. The last term in Eq. (9) is the nonlocal gradient correction with $x_\sigma(\boldsymbol{r}) = |\nabla\rho_\sigma(\boldsymbol{r})|/\rho_\sigma^{4/3}(\boldsymbol{r})$, which ensures the proper long-range Coulombic asymptotic potential $v_{\mathrm{xc},\sigma}^{\mathrm{LB94}} \to -1/r$ as $r \to \infty$. Note that if the conventional XC energy functional forms taken from the LSDA or generalized gradient approximation (GGA) [45,46] are used, the corresponding XC potential $v_{\mathrm{xc},\sigma}(\boldsymbol{r},t)$ will not possess the correct long-range asymptotic $(-1/r)$ behavior [47]. For the time-independent case, this van Leeuwen–Baerends exchange-correlation potential has been found to be reliable for atomic and molecular DFT calculations [19,31,38–41,48–50].

The H_2 molecules' high-order-harmonic generation (HHG) power spectra can be investigated accurately and efficiently by solving the three-dimensional (3D) TDDFT in space and time by means of the time-dependent generalized pseudospectral (TDGPS) method [51] in prolate spheroidal coordinates [28,50,52]. Once the time-dependent wave function $\psi(\xi,\eta,t)$ is available, we can calculate the expectation value of the induced dipole moment in acceleration form,

$$d_A(t) = \sum_{i\sigma} < \psi_{i\sigma}(\xi,\eta,t)|\nabla V_{\mathrm{n}}(\xi,\eta)|\psi_{i\sigma}(\xi,\eta,t) > -E(t). \tag{10}$$

The HHG power spectra $S(\omega)$ (spectral density of the radiation energy) in the acceleration form can be obtained by the Fourier transformation of the time-dependent dipole moment in acceleration form $d_A(t)$,

$$S(\omega) = \frac{2}{3\pi c^3}\left|\int_{-\infty}^{\infty} d_A(t)\exp(i\omega t)dt\right|^2. \tag{11}$$

Figure 1(a) shows the HHG power spectrum of the H_2 molecule along with a time-domain superposition of the harmonics 9–15 in Fig. 1(b). The HHG power spectrum of the H_2 molecule ($R = 1.4a_0$) was calculated by TDDFT equations for diatomic molecules with a proper long-range potential (LB94) [31] in an intense NIR laser field. In all calculations, we adopt a 1064 nm NIR laser wavelength and the laser has a sine-squared pulse shape with a duration of 20 optical cycles (for 1064 nm wavelength, 1 optical cycle = 3.55 fs). The driving laser intensity is $I = 7\times10^{13}$ W/cm^2. The corresponding Keldysh parameter γ is equal to 1.02 ($\gamma = \sqrt{I_p/2U_p}$), which indicates an intermediate ionization regime (multiphoton ionization is

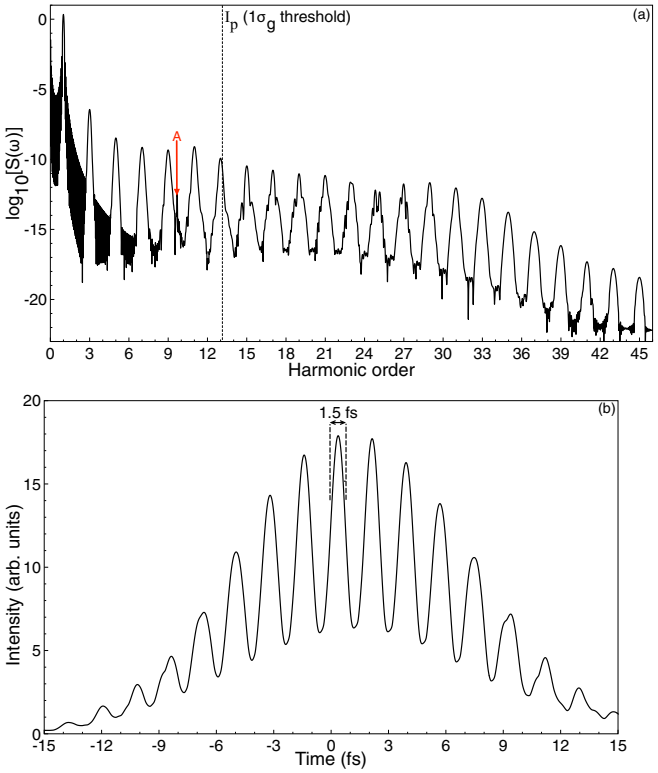

FIG. 1. (a) The HHG power spectrum of H_2 ($R = 1.4a_0$) driven by an intense 1064 nm (near-infrared) laser pulse with the peak intensity $I = 7\times10^{13}$ W/cm^2. The black vertical dashed line indicates the corresponding ionization threshold marked by I_p ($1\sigma_g$). Resonance A corresponds to excitation of the $1\sigma_u$ state. (b) A time-domain superposition of the harmonics 9–15 [which are below-threshold (nonresonant and resonant; harmonic order 9.73) and near-threshold harmonics]. Note that the maximum burst has a duration of about 1.5 fs.

typically characterized by $\gamma > 1$, while tunneling ionization is typically characterized by $\gamma < 1$). Near- and below-threshold harmonic generation provides a potential approach to generate a vacuum-ultraviolet frequency comb [6]. Note that in Fig. 1(b) the maximum burst has a duration of about 1.5 fs. To obtain the induced dipole acceleration and HHG spectra used in the calculations, we set the grid size (for the ξ and η coordinates, respectively) to 70×30. We use 4096 time steps per optical cycle (81 920 steps for the total pulse of 20 optical cycles) in the time propagation process.

B. *Ab initio* TDSE simulation of the H_2 molecule

The time-dependent electron wave function $\psi(\boldsymbol{r},t)$ of H_2 at a fixed internuclear distance satisfies the TDSE with use of a model potential $V_{\rm mod}(\xi,\eta)$:

$$i\frac{\partial}{\partial t}\psi(\boldsymbol{r},t) = [H_0(\boldsymbol{r}) + V_{\rm laser}(\boldsymbol{r},t)]\psi(\boldsymbol{r},t). \tag{12}$$

Here, $H_0(\boldsymbol{r})$ is the unperturbed electronic Hamiltonian,

$$H_0(\boldsymbol{r}) = -\tfrac{1}{2}\nabla^2 + V_{\rm mod}(\xi,\eta). \tag{13}$$

$V_{\rm mod}(\xi,\eta)$ is the H_2 model potential (which includes the H_2 molecules' nuclear, Hartree, and exchange-correlation potentials) [53] constructed from the DFT calculation with use of the $LB94$ exchange-correlation potential,

$$V_{\rm mod}(\xi,\eta) = V_{\rm eff}(r_1) + V_{\rm eff}(r_2), \tag{14}$$

where $r_1(r_2)$ is the distance between the active electron and nucleus one (two). $V_{\rm eff}$ has the following form:

$$V_{\rm eff}(r) = -\frac{\alpha + \beta e^{-\sigma r}}{r}, \tag{15}$$

with $\alpha = 0.5$, $\beta = 0.5$, and $\sigma = 1.78$ calculated by the least-squares fitting of the converged DFT calculation using the nuclear [v_n; Eq. (7)], Hartree [$v_{\rm H}$; Eq. (4)], and LB94 exchange-correlational [$v_{\rm xc}^{\rm LB94}$; Eq. (9)] potentials ($V_{\rm mod} = v_n + v_{\rm H} + v_{\rm xc}^{\rm LB94}$). This constructed model potential $V_{\rm mod}(\xi,\eta)$ will be used later (Sec. III) in the extended semiclassical calculations of the H_2 molecule in an intense NIR laser field.

III. RESULTS AND DISCUSSION

A. SST time-frequency analysis and semiclassical trajectories

To analyze the underlying mechanism from the *ab initio* simulation, we perform the SST time-frequency analysis of the dipole acceleration for H_2 interacting with the applied laser field. In previous studies [32], several representative time-frequency methods have been compared for the atomic hydrogen system, including the short-time Fourier transforms, such as Gabor transform, Wigner-Ville transform [33], and the SST [24,25], as well as the continuous wavelet transform, the bilinear time-frequency transform, and the reallocation method, respectively. They found that both the Gabor and the Morlet transforms are subject to some obscure spectral features arising from a window and that the Wigner-Ville transform is accompanied by interference artifacts, resulting in incomprehensible analysis. Among these methods, only the SST can resolve the intrinsic blurring in the Gabor and the Morlet transforms [34]. As a result, we adopt the SST to explore the characteristic behaviors of harmonic spectra below the ionization threshold, which has successfully depicted chronotaxic systems [35] and cardiovascular systems [54]. We perform the time-frequency analysis on the induced dipole moment in acceleration form $d_A(t')$ of the H_2 diatomic molecule interacting with the applied laser field by means of the synchrosqueezing transform (SST) [32,34]. The SST is described as

$$S(t,\xi) = \int \frac{1}{\sqrt{\omega}} V(t,\omega) \frac{1}{\alpha\sqrt{\pi}} \exp\left\{-\left[\frac{\xi - \Omega_f(t,\omega)}{\alpha}\right]^2\right\} d\omega, \tag{16}$$

where $V(t,\omega)$ is the Morlet wavelet transform, $\Omega_f(t,\omega)$ is the reallocation rule function, and α is a smoothing parameter. In this study, $\alpha = 2.6$. The Morlet wavelet transform is given as

$$V(t,\omega) = \int d_A(t')\sqrt{\omega} W[\omega(t'-t)]dt', \tag{17}$$

where

$$W(x) = \frac{1}{\sqrt{\tau}} \exp(ix) \exp\left(-\frac{x^2}{2\tau^2}\right) \tag{18}$$

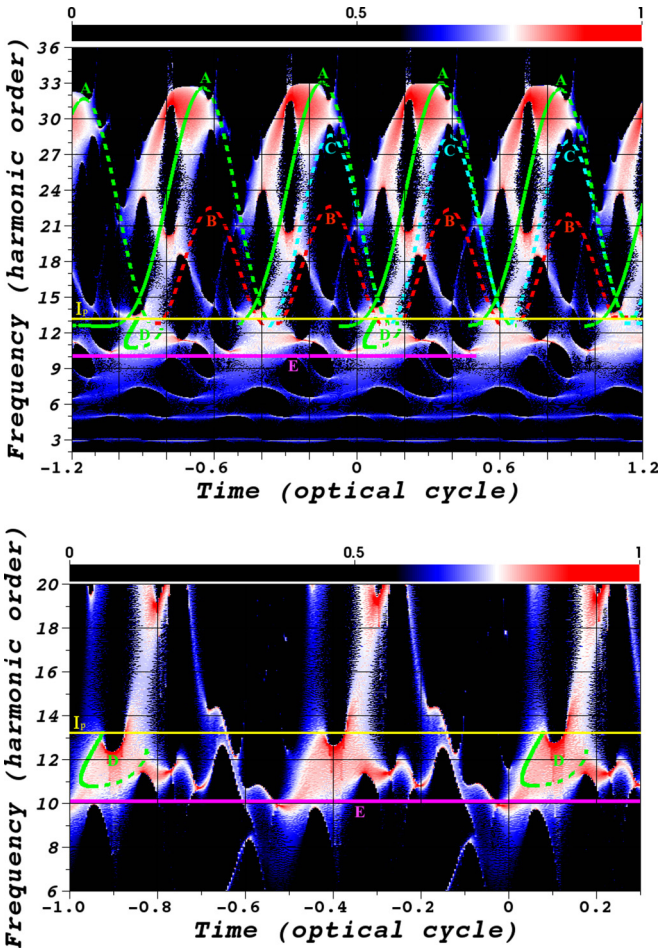

FIG. 2. Upper panel: SST time-frequency analysis of the HHG spectra of H_2. For comparison, the green curves labeled A [both solid lines (short trajectories) and dashed lines (long trajectories)], red curves labeled B [dashed lines (multirescattering trajectories)], and light-blue curves labeled C [dashed lines (multirescattering trajectories)] indicate the semiclassical trajectories for the first, second, and third return, respectively. The magenta line labeled E indicates the semiclassical below-threshold resonant trajectories, which corresponds to the bound-bound transition from $1\sigma_g - 1\sigma_u$ near H10. The yellow solid line indicates the ionization potential I_p. Lower panel: An enlarged view of the SST time-frequency profiles in the near- and below-threshold regions comparing the below-threshold semiclassical trajectories for the first return [green curves labeled D; both solid lines (short trajectories) and dashed lines (long trajectories)]. The laser parameters used are the same as those in Fig. 1. These semiclassical trajectories are also shown in Fig. 3.

is the mother wavelet. The reallocation rule function is defined as

$$\Omega_f(t,\omega) = \begin{cases} \frac{-i\partial_t V(t,\omega)}{V(t,\omega)} & \text{for } V(t,\omega) \neq 0 \\ \infty & \text{for } V(t,\omega) = 0, \end{cases} \tag{19}$$

where ∂_t denotes the partial derivative in the temporal axis.

The time-frequency representation in Fig. 2 shows a periodic repetition of arches comprising the short and long trajectories. It is readily observed that the main contribution to the above-threshold harmonics is due to the short trajectories. The prominent trajectory located near the vicinity of the 10th harmonic is the $1\sigma_g$–$1\sigma_u$ multiphoton resonance transition of H_2. To explore the dynamical role of the quantum trajectories, we extend a standard semiclassical approach, suggested independently by Corkum [13] and Kulander *et al.* [14], with the inclusion of the molecular potential. The initial condition is that the electrons are initially released at either the left or right hydrogen core with the initial velocity along or opposite the polarization direction of the laser field. In our calculation, the semiclassical results are obtained by solving the Newton's equation including the molecular potential ($V_{\rm mod}$) given by Eq. (14), which is

$$\ddot{\mathbf{r}} = -\nabla V_{\rm mod} - E(t)\mathbf{e}_z, \tag{20}$$

where $E(t)$ is the electric-field strength of the laser field and $V_{\rm mod}$ is the H_2 molecules model potential [Eq. (14)] constructed from the DFT method with use of the LB94 exchange-correlation potential.

Here the electric-field force corresponding to the applied laser field in atomic units is $\mathbf{F}_z = E(t)\mathbf{e_z}$, where $\mathbf{e_z}$ is the unit vector in the z direction and $E(t)$ is the electric field of the laser pulse. For the laser parameters used, the corresponding Keldysh parameter γ is $\sim$1, which indicates an intermediate ionization regime; the initial conditions (multiphoton) are provided by releasing the electrons with an initial velocity (v_0) to overcome a potential barrier. Therefore, the direction of the initial velocity of electrons is either "identical" or "opposite" with respect to $\mathbf{F}_z$.

The semiclassical return energy as a function of the ionization time and return time of the electrons that are released in the first couple of cycles before and after the pulse peak for identical conditions are presented in Fig. 2 overlaying the SST time-frequency analysis. We indicate the short and long trajectories as those in the standard three-step model, as well as the multirescattering trajectories (second and third return) and resonant trajectories. In Fig. 2, by comparing with the classical calculation, it is clearly seen that the multirescattering trajectories has strong contributions to the below-, near-, and above-threshold harmonics 10–32. This SST result (Fig. 2) is in good agreement with the extended semiclassical returning energy map result shown in Fig. 3. In Fig. 3, we calculate the probability of the electrons with the corresponding return time t and return energy E by using an extended semiclassical method [55], which can be obtained from the following expression:

$$\frac{dP(E,t)}{dEdt} = \int dt' d\mathbf{v} W[|E(t')|] P(\mathbf{v}) C_t(t', \mathbf{r}_0, \mathbf{v}, E_r, t_r) \times \delta(E - E_r)\delta(t - t_r), \tag{21}$$

where $W[|E(t')|]$ is the instantaneous tunneling ionization rate, E_r and t_r are the returning time and returning energy (kinetic energy + potential energy) for given trajectories, and $P(\mathbf{v})$ are the Gaussian initial velocity distributions. Each trajectory is monitored for all the approaches to either of the hydrogen cores ($z = \pm 0.7$ a.u.) for the H_2 molecule. If an electron trajectory is such that it can return to either of the hydrogen cores at time t_r with a returning energy E_r, the factor $C_t(t', \mathbf{r}_0, \mathbf{v}, E_r, t_r)$ is set to 1. Otherwise, $C_t(t', \mathbf{r}_0, \mathbf{v}, E_r, t_r) = 0$. In Fig. 3, it is clearly seen that several multirescattering trajectories (m2, m3, and m4, which are the second, third,

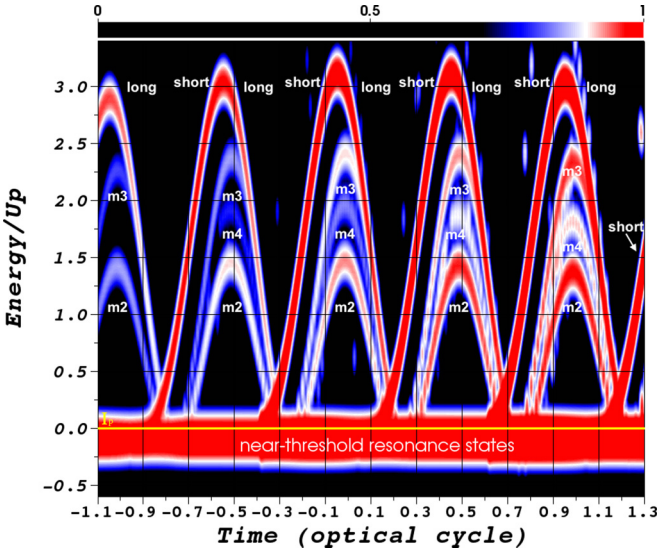

FIG. 3. Semiclassical returning energy map. Note that the probability of the electrons with the corresponding return time and return energy is calculated by using an extended semiclassical method introduced in Refs. [36,55]. The yellow solid line indicates the ionization potential I_p. The first return long and short trajectories are labeled along with m2, m3, and m4, which are the second, third, and fourth multirescattering returns for the long trajectories, respectively. The dense red horizontal line in the density plot near the I_p is the near-threshold resonance states calculated by the extended semiclassical method. The laser parameters used are the same as those in Fig. 1.

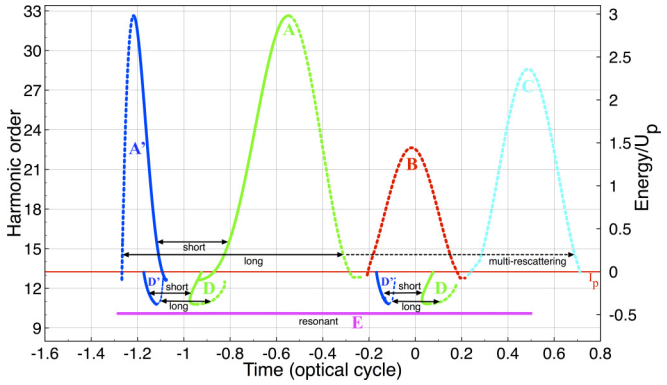

FIG. 4. Semiclassical return energy as a function of ionization times (labeled A' and D') and return times (labeled A–E). The solid and dotted colored lines represent the short and long trajectories, respectively. Here we can see the multirescattering of the long trajectories at different return times. For clarity, we show the semiclassical return energy as a function of ionization time (labeled A' and D'; blue line), first return time (labeled A; green dashed and solid line), second return time (labeled B; red dashed line), and third return time (labeled C; light-blue dashed line) for the electrons released before the pulse peak. Several typical rescatterings are marked by black text, hence, short, long, multirescattering, and resonant trajectories (labeled E; magenta line). Here the initial condition is that the electrons with an initial velocity v_0 are released from the left-side hydrogen core ($z = -0.7$ a.u.) along the electronic-field force $\mathbf{F}_z$. The laser parameters used are the same as those in Fig. 1.

and fourth multirescattering returns for the long trajectories, respectively) are superposed before and after the peak of laser field.

B. Electron dynamics in below-, near-, and above-threshold HHG

To explore the intricate structures in the below-, near-, and above-threshold harmonic generation, we show the semiclassical return energy as a function of ionization times and return times in Fig. 4. Note that the returning energy includes the kinetic energy and the potential energy, and thus may become negative below the ionization threshold. It is clearly seen that the HHG originated from three quantum trajectories, namely, the short and long trajectories and also the below-threshold resonant trajectories. In Fig. 4, the trajectories that lie between the harmonic 13 and 29 suggest multiple returns of the electron. We find that the long-trajectory electrons associated with the multirescatterings contribute to the below-, near-, and above-threshold harmonics 13–29, and the corresponding travel time is about one optical cycle. The trajectories in Fig. 4 are superimposed in Fig. 2 for the sake of comparison with the SST representation. As shown in the figures, the structures of the SST representation are in agreement with the semiclassical trajectories for below-, near-, and above-threshold harmonics and the resonant excited state.

The contribution of quantum trajectories to the below-, near-, and above-threshold harmonic generation can be understood according to Figs. 2–4. Power *et al.* [16] pointed out recently that long trajectories are the favored pathways in below- and near-threshold harmonic generation. The more recent study by Li *et al.* [24–26] on atomic systems and our present study of H_2 diatomic molecule and SST time-frequency analysis further show that these long trajectories are, in fact, the multirescattering trajectories. In the below-threshold region seen from Fig. 2, extrapolated from the overlaying semiclassical result, we can say short and long trajectories have even contributions to harmonics 11–13, and the resonant trajectories contribute to harmonics near H10 (9.73). For above-threshold harmonics, the short and multirescattering trajectories have the major contributions. Note that in Fig. 2, the strongest resonant emissions (∼H10) for each of the optical cycles are located near the laser peak intensity.

To explain the detailed electronic dynamic behaviors in the near- and below-threshold generation, the positions of the electrons as a function of the time are shown in Figs. 5(a)–5(c) and Figs. 6(a) and 6(b). For the near-threshold long trajectories [Fig. 5(a)], the electron first tunnels through the lower part of the barrier potential (leaving the core near maximum of the laser field), accelerates, and returns to the left-side ($z = -0.7$ a.u.) or right-side ($z = 0.7$ a.u.) hydrogen core. This is a typical tunneling process. Nevertheless, when the electron once again returns to the left- or right-side hydrogen core, it now faces the combined molecule-field potential wall [the higher part of the barrier potential (HBP) on the other side] and tunneling is unlikely. Thus the electron first moves towards the HBP and subsequently absorbs several photons to a higher-energy state and quickly returns to the ground state, unless the return energy is greater than zero. Such a mechanism

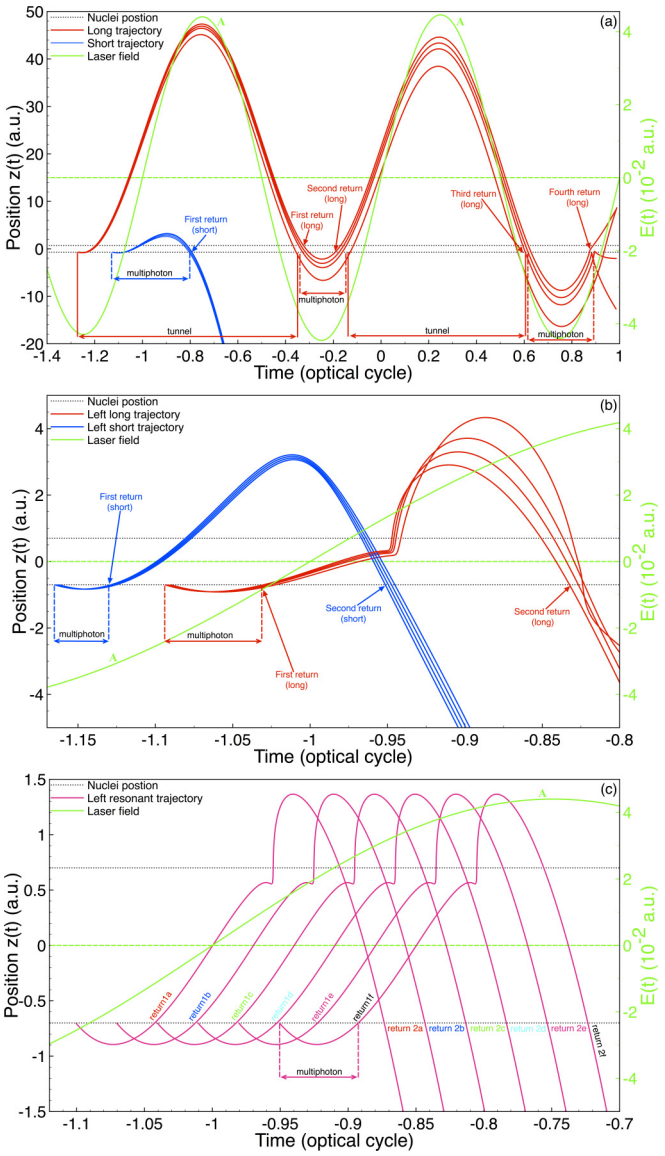

FIG. 5. Semiclassical trajectories for below- and near-threshold harmonics. Position vs time for (a) near-threshold, (b) below-threshold (nonresonant and resonant), and (c) below-threshold (resonant) regions for the corresponding return energies shown in Fig. 4. The black horizontal dashed line indicates the position of the two hydrogen nuclei ($z = \pm 0.7$ a.u.) for H_2. Here the initial condition is that the electrons with an initial velocity v_0 are released from the left-side hydrogen core ($z = -0.7$ a.u.) along the electronic-field force $\mathbf{F}_z$. The green solid line (labeled A) indicates the corresponding laser field, and the laser parameters used are the same as those in Fig. 1.

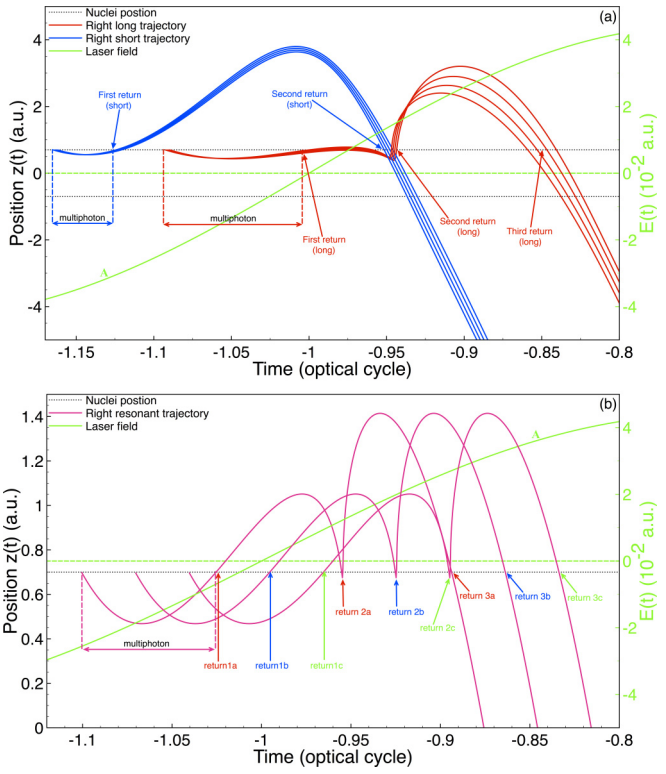

FIG. 6. Semiclassical trajectories for below- and near-threshold harmonics. Position vs time for (a) below-threshold (nonresonant and resonant) and (b) below-threshold (resonant) regions for the corresponding return energies shown in Fig. 4. The black horizontal dashed line indicates the position of the two hydrogen nuclei ($z = \pm 0.7$ a.u.) for H_2. Here the initial condition is that the electrons with an initial velocity v_0 are released from the right-side hydrogen core ($z = 0.7$ a.u.) along the electronic-field force $\mathbf{F}_z$. The green solid line (labeled A) indicates the corresponding laser field, and the laser parameters used are the same as those in Fig. 1.

is similar to the multiphoton process. The near-threshold long-trajectory electrons have multiscattering behaviors, and the first return has a travel time around 0.8–1.0 optical cycle, as seen in Figs. 4 and 5(a). However, the multirescattering process has a longer travel time (∼1.3 optical cycles). Indeed, to end the first return of the long trajectories in Fig. 5(a) (labeled first and second return), the electrons still move along the electric field, which allows them to quickly return to the core at near the peak intensity in ∼0.14 optical cycles. The near-threshold short trajectory (first return) has a different mechanism, where the electron leaves the core near the zero laser fields and always faces the HBP, where tunneling ionization is impossible. As a result, the electron leaves the left-side hydrogen core ($z = -0.7$ a.u.) and collides with the right-side hydrogen core ($z = 0.7$ a.u.) within 0.15 optical cycles due to the molecular potential force exerted from the right hydrogen core. It is then pulled back to the core it was released from [left-side hydrogen core ($z = -0.7$ a.u.)] quickly by the molecular potential. This behavior only involves the multiphoton process. In Fig. 5(a), the near-threshold short-trajectory electrons are allowed to quickly revisit the core with a short travel time (around 0.35 optical cycles), which nearly coincides with the local peak of the laser field (see the green solid line). The near-threshold short-trajectory dynamics of H_2 molecules involves mainly the multiphoton process, which is different from that of the atomic cases, where the tunneling mechanism dominates [24–26]. Also, for near- and above-threshold short and long trajectories, the return time and dynamics for electrons leaving the right- or left-sided hydrogen core are very similar. This is not the case for the below-threshold trajectories, where different dynamics play a role depending on which hydrogen core (left or right) the electron initially leaves from.

Next, we unveil the electronic dynamic behaviors for below-threshold harmonics and take into consideration which hydrogen core the electron was released from since the dynamics are very different. We will focus on the below-threshold dynamics that are released and returned within $-1.2 \leqslant T \leqslant -0.8$ optical cycles, which can be seen in the SST (Fig. 2) and semiclassical (Fig. 4) representations. In Fig. 5(b), we show the positions of the electrons as a function of time for below-threshold long and short trajectories that are released from the left-side ($z = -0.7$ a.u.) hydrogen core, and in Fig. 6(a), we show the trajectories that are released from the right-side ($z = 0.7$ a.u.) hydrogen core. The short and long trajectories that are released from the left-side hydrogen core have mainly two returns, due to the molecular potential force exerted from the right hydrogen core. When the electrons are released from the right-side hydrogen core [Fig. 6(a)], the long and short trajectories have three returns and two returns, respectively. The below-threshold HHG long and short electron trajectories are both associated with multiple rescatterings. This is very different from the above-threshold HHG dynamics where only long trajectories are associated with multiple rescatterings. In Figs. 5(b) and 6(a), for both long and short electron trajectories, the electron absorbs several photons and travels a small distance away (<4.5 a.u.) from the core and is pulled back to the core quickly by the molecular potential; this behavior only involves the multiphoton process. This behavior is observed for each of the multiple returns. For the short and long trajectories' first return, the electrons are released and absorb nearly 10 photons and return very quickly back to the core (travel time <0.09 optical cycles). Upon their first return, the long and short trajectories emit ~10 photons, which is equivalent to the resonant energy between the $1\sigma_g - 1\sigma_u$ states. After the first return, the long and short trajectories have a longer travel time, corresponding to 0.26 and 0.21 optical cycles, respectively. Upon their second return, the long and short trajectories emit photons with an energy in the range of 10.5 $\leqslant$ harmonic orders $\leqslant$13.2 (seen in Figs. 2 and 4). Here, as seen in Fig. 5(b), the below-threshold harmonics in the range of 10.5 $\leqslant$ harmonic orders $\leqslant$13.2 are heavily affected by the $1\sigma_g$–$1\sigma_u$ excited-state resonance near the 10th harmonic order. Furthermore, below-threshold harmonics near excited-state resonances will behave differently (here, causing trajectories to have multiple returns) than harmonics that have no neighboring resonances.

Lastly, in Figs. 5(c) and 6(b), we investigate resonant trajectory dynamics in the below-threshold HHG. We will focus on the dynamics of the resonant trajectories (which correspond to the bound-bound transition from $1\sigma_g$–$1\sigma_u$) that are released and returned within $-1.1 \leqslant T \leqslant -0.7$ optical cycles, which can be seen in the SST (Fig. 2) and semiclassical (Fig. 4) representations. Figure 5(c) (released from left core) and Fig. 6(b) (released from right core) shows several below-threshold resonant trajectories. The resonant trajectories' dynamics are as follows: the electrons absorb nearly 10 photons and are excited, but return quickly to the left core (right core), with a travel time ~0.06 (~0.08) optical cycles. For the time domain ($-1.1 \leqslant T \leqslant -0.7$ optical cycles) shown in Figs. 5(c) and 6(b), when the electron is released from the left-side hydrogen core, the force exerted on it drives it to the right-side hydrogen core [Fig. 5(c)] where the electron is highly attracted by the right-side hydrogen core. When the electron is released from the right-side hydrogen core [Fig. 6(b)], the force exerted on it drives it away from the right side in the opposite direction from the right- or left-side hydrogen core ($z \geqslant 0.7$ a.u.), where there is minimal influence from the opposite core (left). This is why there are more returns (multirescattering) and a longer travel time for the long and short trajectories that are released from the right-side hydrogen core. The opposite would be the case if we were to look at the next half optical cycle (hence, $-0.7 \leqslant T \leqslant -0.3$ optical cycles).

IV. CONCLUSION

In this paper, we have presented a detailed investigation and analysis of a regime of below-, near-, and above-threshold harmonic generation of H_2 molecules in an intense NIR laser field. We have performed a quantum trajectories' analysis of the below-, near-, and above-threshold harmonics by using the SST time-frequency profiles and identified the trajectories with the assistance of an extended semiclassical simulation. Several dynamical features of various quantum trajectories, including short, long, multirescattering, multiphoton, resonance, etc., associated with the below-, near- (ionization), and above-threshold harmonics of the two-center molecular system are uncovered. We find that multiphoton-dominated short trajectories, long trajectories, multirescattering trajectories, and resonant trajectories in the below- and near-threshold HHG involve only the electron scattered off the combined molecule-field potential wall followed by the absorption of photons. Also, we find that the multiphoton-dominated processes for the long trajectories only occur when the electrons are scattered off the high part of the combined molecule-field barrier potential (HBP) followed by the absorption of many photons in the below- and near-threshold harmonic generation. In particular, we reveal that short trajectories are multiphoton dominated and can have multiple returns for below-threshold harmonics, and excited-state resonances can have effects on the generation of neighboring below-threshold harmonics. Furthermore, we find that the electron dynamics for below-threshold long, short, and resonant trajectories differ greatly, depending on which hydrogen core (left or right) it was initially released from during a half optical cycle. Our study provides informative findings on the delicate electron dynamics in the near- and below-threshold harmonic regimes for multielectron diatomic molecules. Our results can facilitate the control of the electron quantum paths for the experimental generation of ultrashort and intense coherent light sources and frequency comb source, both in the VUV regime, in the future.

ACKNOWLEDGMENTS

We thank Dmitry A. Telnov, Chon Teng Belmiro Chu, and Peng-Cheng Li for fruitful discussions. This work was partially supported by the Chemical Sciences, Geosciences and Biosciences Division of the Office of Basic Energy Sciences, Office of Sciences, US Department of Energy under Grant No. DE-FG02-04ER15504. We also acknowledge the partial support of the Ministry of Science and Technology of Taiwan and National Taiwan University (Grants No. 106R104021 and No. 106R8700-2).

[1] F. Krausz and M. Ivanov, Rev. Mod. Phys. **81**, 163 (2009).
[2] J. Henkel, T. Witting, D. Fabris, M. Lein, P. L. Knight, J. W. G. Tisch, and J. P. Marangos, Phys. Rev. A **87**, 043818 (2013).
[3] M. Chini, K. Zhao, and Z. Chang, Nat. Photon. **8**, 178 (2014).
[4] M. Hentschel, R. Kienberger, C. Spielmann, G. A. Reider, N. Milosevic, T. Brabec, P. Corkum, U. Heinzmann, M. Drescher, and F. Krausz, Nature (London) **414**, 509 (2001).
[5] J. Itatani, J. Levesque, D. Zeidler, H. Niikura, H. Pepin, J. C. Kieffer, P. B. Corkum, and D. M. Villeneuve, Nature (London) **432**, 867 (2004).
[6] D. C. Yost, T. R. Schibli, J. Ye, J. L. Tate, J. Hostetter, M. B. Gaarde, and K. J. Schafer, Nat. Phys. **5**, 815 (2009).
[7] W. H. Xiong, L. Y. Peng, and Q. Gong, J. Phys. B **50**, 032001 (2017).
[8] S. Haessler, J. Caillat, W. Boutu, C. Giovanetti-Teixeira, T. Ruchon, T. Auguste, Z. Diveki, P. Breger, A. Maquet, B. Carre *et al.*, Nat. Phys. **6**, 200 (2010).
[9] S. Baker, J. S. Robinson, C. A. Haworth, H. Teng, R. A. Smith, C. C. Chirilă, M. Lein, J. W. G. Tisch, and J. P. Marangos, Science **312**, 424 (2006).
[10] E. J. Takahashi, P. Lan, O. D. Mücke, Y. Nabekawa, and K. Midorikawa, Nat. Commun. **4**, 2691 (2013).
[11] M. Drescher, M. Hentschel, R. Kienberger, M. Uiberacker, V. Yakovlev, A. Scrinzi, T. Westerwalbesloh, U. Kleineberg, U. Heinzmann, and F. Krausz, Nature (London) **419**, 803 (2002).
[12] R. Kienberger, M. Hentschel, M. Uiberacker, C. Spielmann, M. Kitzler, A. Scrinzi, M. Wieland, T. Westerwalbesloh, U. Kleineberg, U. Heinzmann *et al.*, Science **297**, 1144 (2002).
[13] P. B. Corkum, Phys. Rev. Lett. **71**, 1994 (1993).
[14] K. C. Kulander, K. J. Schafer, and J. Krause, in *Proceedings of the Workshop on Super-Intense Laser Atom Physics (SILAP) III*, edited by P. Piraux, A. L. Huillier, and J. Rzazewski (Plenum, New York, 1993).
[15] M. Lewenstein, P. Salieres, and A. L'Huillier, Phys. Rev. A **52**, 4747 (1995).
[16] E. P. Power, A. M. March, F. Catoire, E. Sistrunk, K. Krushelnick, P. Agostini, and L. F. DiMauro, Nat. Photon. **4**, 352 (2010).
[17] J. A. Hostetter, J. L. Tate, K. J. Schafer, and M. B. Gaarde, Phys. Rev. A **82**, 023401 (2010).
[18] H. Soifer, P. Botheron, D. Shafir, A. Diner, O. Raz, B. D. Bruner, Y. Mairesse, B. Pons, and N. Dudovich, Phys. Rev. Lett. **105**, 143904 (2010).
[19] M. Chini, X. Wang, Y. Cheng, H. Wang, Y. Wu, E. Cunningham, P.-C. Li, J. Heslar, D. A. Telnov, S. I. Chu, and Z. Chang, Nat. Photon. **8**, 437 (2014).
[20] W.-H. Xiong, J.-W. Geng, J.-Y. Tang, L.-Y. Peng, and Q. Gong, Phys. Rev. Lett. **112**, 233001 (2014).
[21] F. Brizuela, C. M. Heyl, P. Rudawski, D. Kroon, L. Rading, J. M. Dahlström, J. Mauritsson, P. Johnsson, C. L. Arnold, and A. L'Huillier, Sci. Rep. **3**, 1410 (2013).
[22] D. Shafir, B. Fabre, J. Higuet, H. Soifer, M. Dagan, D. Descamps, E. Mevel, S. Petit, H. J. Worner, B. Pons *et al.*, Phys. Rev. Lett. **108**, 203001 (2012).
[23] K. Kato, S. Minemoto, Y. Sakemi, and H. Sakai, Phys. Rev. A **90**, 063403 (2014).
[24] P.-C. Li, Y.-L. Sheu, C. Laughlin, and S. I. Chu, Phys. Rev. A **90**, 041401(R) (2014).
[25] P. C. Li, Y. L. Sheu, C. Laughlin, and S. I. Chu, Nat. Commun. **6**, 8178 (2015).
[26] P. C. Li, Y. X. Jiao, X. X. Zhou, and S. I. Chu, Opt. Express **24**, 14352 (2016).
[27] Y. Nabekawa, Y. Furukawa, T. Okino, A. Amani Eilanlou, E. J. Takahashi, K. Yamanouchi, and K. Midorikawa, Nat. Commun. **7**, 12835 (2016).
[28] J. Heslar, D. A. Telnov, and S. I. Chu, Phys. Rev. A **93**, 063401 (2016).
[29] K. N. Avanaki, D. A. Telnov, and S.-I. Chu, Phys. Rev. A **90**, 033425 (2014).
[30] M. Haertelt, X.-B. Bian, M. Spanner, A. Staudte, and P. B. Corkum, Phys. Rev. Lett. **116**, 133001 (2016).
[31] R. van Leeuwen and E. J. Baerends, Phys. Rev. A **49**, 2421 (1994).
[32] Y. L. Sheu, L. Y. Hsu, H. T. Wu, P. C. Li, and S. I. Chu, AIP Adv. **4**, 117138 (2014).
[33] P. Flandrin, *Time-Frequency/Time-Scale Analysis* (Academic Press, New York, 1999).
[34] Y. C. Chen, M. Y. Cheng, and H. T. Wu, J. R. Stat. Soc. Ser. B Stat. Methodol. **76**, 651 (2014).
[35] Y. F. Suprunenko, P. T. Clemson, and A. Stefanovska, Phys. Rev. Lett. **111**, 024101 (2013).
[36] J. Heslar and S. I. Chu, Sci. Rep. **6**, 37774 (2016).
[37] X. Chu and S. I. Chu, Phys. Rev. A **63**, 023411 (2001).
[38] D. A. Telnov, J. Heslar, and S. I. Chu, in *Theoretical and Computational Developments in Modern Density Functional Theory*, edited by A. K. Roy (Nova Science, New York, 2012), pp. 357–390.
[39] J. Heslar, D. A. Telnov, and S. I. Chu, in *Concepts and Methods in Modern Theoretical Chemistry: Statistical Mechanics*, edited by S. Ghosh and P. Chattaraj (Taylor and Francis, Boca Raton, FL, 2013), Vol. 2, pp. 37–55.
[40] J. Heslar, D. Telnov, and S. I. Chu, Phys. Rev. A **83**, 043414 (2011).
[41] J. Heslar, J. J. Carrera, D. A. Telnov, and S. I. Chu, Int. J. Quantum Chem. **107**, 3159 (2007).
[42] W. Kohn and L. J. Sham, Phys. Rev. **140**, A1133 (1965).
[43] C. A. Ullrich, U. J. Gossmann, and E. K. U. Gross, Phys. Rev. Lett. **74**, 872 (1995).
[44] *Time-Dependent Density Functional Theory*, edited by M. A. L. Marques, C. A. Ullrich, F. Nogueira, A. Rubio, K. Burke, and E. K. U. Gross (Springer, Berlin, 2006).
[45] R. G. Parr and W. Yang, *Density-Functional Theory of Atoms and Molecules* (Oxford University Press, Oxford, 1989).
[46] R. M. Dreizler and E. K. U. Gross, *Density Functional Theory, An Approach to the Quantum Many-Body Problem* (Springer, Berlin, 1990).
[47] X.-M. Tong and S. I. Chu, Phys. Rev. A **55**, 3406 (1997).
[48] S. I. Chu, J. Chem. Phys. **123**, 062207 (2005).
[49] P. R. T. Schipper, O. V. Gritsenko, S. J. A. van Gisbergen, and E. J. J. Baerends, J. Chem. Phys. **112**, 1344 (2000).
[50] D. A. Telnov, J. Heslar, and S. I. Chu, Phys. Rev. A **90**, 063412 (2014).
[51] X. M. Tong and S. I. Chu, Chem. Phys. **217**, 119 (1997).
[52] X. Chu and S. I. Chu, Phys. Rev. A **63**, 013414 (2000).
[53] Y. J. Jin, X. M. Tong, and N. Toshima, Phys. Rev. A. **83**, 063409 (2011).
[54] H. T. Wu, Y. H. Chan, Y. T. Lin, and Y. H. Yeh, Appl. Comput. Harmon. Anal. **36**, 354 (2014).
[55] J. J. Carrera, X. M. Tong, and S. I. Chu, Phys. Rev. A **74**, 023404 (2006).